The Astrophysical Journal, 626:959–965, 2005 June 20

MULTISCALE MAGNETIC FIELDS IN STAR-FORMING REGIONS: INTERFEROMETRIC POLARIMETRY OF THE MMS 6 CORE OF OMC-3

Brenda C. Matthews
Radio Astronomy Laboratory, University of California, Berkeley, CA 94720; bmatthews@astro.berkeley.edu

Shih-Ping Lai
Department of Astronomy, University of Maryland, College Park, MD 20742; slai@astro.umd.edu

Richard M. Crutcher
Department of Astronomy, University of Illinois, Urbana, IL 61801; crutcher@astro.uiuc.edu

and

Christine D. Wilson
Department of Physics and Astronomy, McMaster University, Hamilton, ON L8S 4M1, Canada;
wilson@physics.mcmaster.ca
Received 2004 December 21; accepted 2005 March 8

ABSTRACT

We present the first interferometric observations of linearly polarized emission toward the OMC-3 region of the Orion A cloud. We have observed the MMS 6 protostellar core at 1.3 mm with the Berkeley-Illinois-Maryland Association (BIMA) array, achieving a resolution of $4\farcs3 \times 3\farcs0$. We find that the polarization angle measured changes systematically across the core, orienting along a dust extension to the northwest. The polarization angle is oriented similarly to the 850 and 350 μm polarized emission measured by the SCUBA and Hertz polarimeters. A polarization hole is detected, as is typical of polarized emission data toward cores. Since the BIMA data are insensitive to structure on spatial scales of $>40''$, the emission detected is dominated by the core and not the integral-shaped filament in which it is embedded. Observations of CO $J = 2-1$ reveal CO emission potentially associated with the core, but no outflow signature is detected. Utilizing the Chandrasekhar-Fermi method, we have used the dispersion in the polarization vectors to estimate a field strength of 640 μG in the plane of the sky, assuming a corrective Q-factor of 0.5. Applying the recent measurement of the inclination of the field to the line of sight (Houde et al.), a total field strength of 680 μG is derived. Despite highly nonthermal line widths, the kinetic energy density is found to be insufficient to support this core against gravitational collapse. The magnetic energy density, when combined with the predominantly turbulent kinetic energy density, is comparable to the effects of gravity, but its value is highly dependent on the applied Q-factor to a degree that the core may be subcritical or supercritical. The preservation of the field geometry from large to small scales in this core is consistent with observations of a second protostellar core in a filamentary cloud in Orion B.

Subject headings: ISM: clouds — ISM: individual (OMC-3 MMS 6) — ISM: magnetic fields — ISM: molecules — polarization — stars: formation

1. INTRODUCTION

Observational evidence suggests that magnetic fields are present in molecular cloud cores at sufficient strengths to provide support against gravitational collapse long enough for fragmentation to occur (Crutcher 1999). However, the regions in which magnetic fields are expected to dominate gravitational forces (i.e., on the large scales of molecular clouds and in uncollapsed cores) are the very regions toward which the field is most difficult to measure due to technical constraints and/or low flux density. Hence, what we know of magnetic fields in molecular clouds comes from measurements of massive collapsed regions, e.g., OMC-1 (Rao et al. 1998) and W51 (Lai et al. 2001), or protostellar cores also undergoing collapse, e.g., NGC 1333 IRAS 4A (Girart et al. 1999) and NGC 2024 FIR 5 (Lai et al. 2002). The few measurements of field strengths are restricted to bright cores with detections of 80 μG (NGC 2024; Crutcher et al. 1999a) to 360 $\pm$ 80 μG (OMC-1; Crutcher et al. 1999b). These Zeeman-splitting measurements do not coincide with regions in which larger scale fields have been measured via dust polarimetry, such as the integral-shaped filament in Orion A (Houde et al. 2004; Matthews et al. 2001) and the molecular ridge in Orion B (Matthews et al. 2002; Dotson et al. 2000). These filaments are still overdense compared to the bulk of molecular cloud material by at least a factor of 10 and also show evidence of complex field geometries, which makes even the estimators of field strength difficult to apply without modeling and making assumptions about field geometry.

It is therefore reasonable to question how well the available data for collapsing cores trace large-scale field strengths and orientations. Is the field of the star-forming cloud preserved in the cores, and if not, how quickly does a core become distinct? Recent observations of the Barnard 1 cloud in Perseus from the Submillimeter Common-User Bolometric Array (SCUBA) at the James Clerk Maxwell Telescope (JCMT) reveal that three of the four cores exhibit a different "mean field" direction[1] from the field of the ambient cloud (Matthews & Wilson 2002). On the other hand, observations in Orion B of the NGC 2024 FIR 5 core at high resolution with the Berkeley-Illinois-Maryland Association (BIMA) interferometer (Lai et al. 2002) reveal a polarization pattern consistent with the JCMT single-dish observations (Matthews et al. 2002) along the same line of sight. The BIMA data are only sensitive to the compact structure of the core, while

[1] Derived by assuming a magnetic field direction orthogonal to the polarization direction, as predicted for individual grains (Hildebrand 1988).

the SCUBA data along the NGC 2024 ridge detect dust throughout the cloud; this suggests that the magnetic field of the parent filamentary cloud has been preserved to much smaller scales. We note that these two data sets also indicate that field tangling on the scale of the BIMA data (with a resolution of $\sim$700 AU for Orion B at 450 pc) is not responsible for the diminished fractional polarization observed toward the position of the core relative to the lower density ridge.

The MMS 6 core is embedded in the OMC-3 region of the integral-shaped filament of Orion A. It is the brightest core detected in the region at both 850 μm (Johnstone & Bally 1999) and 1300 μm (Chini et al. 1997). Reipurth et al. (1999) identify a 3.6 cm source at the position of MMS 6, indicating the presence of free-free emission, which can be produced by shocks in outflowing material from a protostar. One of two suspected Herbig-Haro flows in the region is associated with MMS 6 (Yu et al. 1997, 2000). However, a search for outflows in OMC-2/3 in the $H^{13}CO^+$ $J = 1-0$, HCO^+ $J = 1-0$, and CO $J = 1-0$ lines by Aso et al. (2000) did not identify one associated with MMS 6. Recent CO $J = 1-0$ observations from the Five College Radio Astronomy Observatory (FCRAO) and BIMA also failed to detect evidence of an outflow from this source (Williams et al. 2003). The only other core without an observed outflow in OMC-3 is MMS 1.

In § 2, we present the observations and explain the data reduction. In § 3, we present our continuum and CO $J = 2-1$ results for MMS 6 and compare them with the larger scale data for the integral-shaped filament. Finally, in § 4, we discuss the implications of the single-dish and high-resolution interferometric data and derive an estimate of the magnetic field strength. We summarize our findings in § 5.

2. OBSERVATIONS AND DATA REDUCTION

The observations of MMS 6 (R.A. = $05^h35^m23^s.489$, decl. = $-05^\circ01'32''.221$[J2000.0]) were made using the BIMA array (Welch et al. 1996) during two epochs (2000 November–December, with completion in 2002 October). Nine BIMA antennas with 1 mm SIS receivers and quarter-wave plates were used. The digital correlator was set up to observe the 1.3 mm continuum with a 750 MHz window in the lower sideband (centered at 226.6 GHz) and a 700 MHz window in the upper sideband (centered at 230.6 GHz). The CO $J = 2-1$ line was simultaneously observed in an isolated 50 MHz window in the upper sideband. The primary beam of the BIMA antennas is approximately 50″ at 1.3 mm, and the synthesized beam of the final maps was $4''.3 \times 3''.0$. Data were obtained in the C-array configuration that has projected baselines between 5 and 68 kilowavelengths. The total on-source integration time was 15.3 hr in five separate tracks.

The process of obtaining and reducing BIMA polarimetry data is described in Matthews (2003) and Rao (1999). Briefly, polarimetry is performed at BIMA utilizing quarter-wave plates in front of the linearly polarized receiver on each antenna to detect left-circularly polarized (LCP) and right-circularly polarized (RCP) radiation. Four cross-correlations on each baseline (LL, RR, LR, and RL) must be measured to obtain all four Stokes parameters (I, Q, U, and V). Ideally, the measurements of L and R would be made simultaneously on each antenna, but since the BIMA antennas each have only one receiver, the polarization plates must be switched out in front of the receivers on a timescale that is shorter than the u-v cell transit time. This switching results in quasi-simultaneous measurements. We used a Walsh switching pattern derived by Rao (1999) to maximize the efficiency of obtaining the cross-correlations. Sixteen switch patterns were required. Since the integration time on each was 11.5 s and the plate switch requires an additional 2–3 s, the total time for one cycle was just under 4 minutes.

Data reduction was done using standard tasks in the MIRIAD software package (Sault et al. 1995). In addition to flagging and phase and flux calibration, polarization data must be calibrated to account for leakage between the two orthogonal polarizations, because the quarter-wave plates do not perfectly sample a single polarization direction. The derivation of the leakage terms from RCP to LCP and vice versa was achieved using observations of 3C 279 over an entire track (4–5 hr) during both epochs. The average leakage per antenna was 4.6% ± 0.4% in 2000 and 5.0% ± 0.4% in 2002. The leakage correction derived for each antenna was applied to the visibility data before the data were inverted to create maps.

To achieve a compromise between resolution and signal-to-noise ratio (S/N), a Briggs weighting factor of 0.5 was used to produce the Stokes I image. The synthesized beam has a half-power beamwidth (HPBW) of $4''.3 \times 2''.95$, with P.A. = 18°. The Stokes Q and U images were produced with natural weighting to maximize the S/N. The resulting images have a HPBW of $4''.8 \times 3''.1$, with P.A. = 12°. All images were deconvolved and cleaned. The resulting cleaned Q and U images were binned to half-beamwidth pixels ($1''.5 \times 2''.5$ in R.A. and decl.) to reduce oversampling. The data were then combined to calculate the linearly polarized intensity,

$$I_p = \sqrt{Q^2 + U^2}, \tag{1}$$

and the polarization position angle,

$$\phi = \frac{1}{2} \arctan \frac{U}{Q}. \tag{2}$$

Combined with a binned Stokes I map, the polarization percentage is calculated as $p' = 100(I_p/I)$. Because the polarization percentage is forced to be positive, a further correction is made to debias the initial results, which overestimate the polarization percentage. Hence, the debiased polarization percentage, p, is given by

$$p = \sqrt{(p')^2 - (dp)^2}, \tag{3}$$

where dp is the uncertainty in the polarization percentage derived from the uncertainties in the polarized intensity and the total intensity:

$$dp = p' \sqrt{\frac{(dI_p)^2}{I_p^2} + \frac{(dI)^2}{I^2}}, \tag{4}$$

where the uncertainty in the polarized intensity is $dI_p = dQ$, under the assumption that $dQ = dU = dV$. Typically, the rms levels in the Q and U maps are best estimated from the Stokes V map, since star-forming regions do not produce significant circularly polarized emission in dust, and the Stokes V map can be assumed to be purely a noise map.

CO $J = 2-1$ data at 230 GHz were obtained over 50 MHz of bandwidth and with a velocity channel width of 1.016 km s^{-1}. These data were continuum subtracted using the continuum

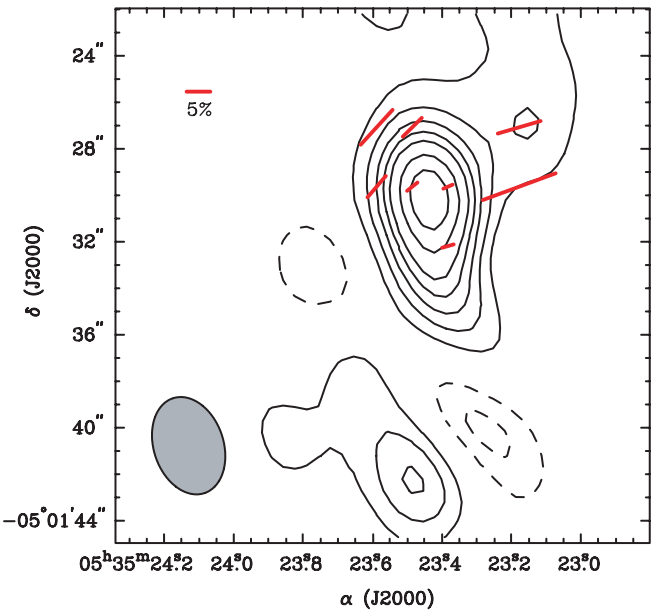

FIG. 1.—Polarization vectors detected in the continuum at 1.3 mm toward MMS 6. The Stokes I intensity map is shown in contours of 3, 6, 9, 12, 15, 20, and 25 σ, where $\sigma = 17$ mJy beam^{-1}, the rms of the cleaned map. Vectors have been produced at positions where $I/\sigma_I > 3$ and $I_p/\sigma_{I_p} > 3$, where I_p is given by eq. (1). The polarization orientations shown correspond to the electric field vector directions as measured. A systematic increase in polarization position angle is evident across the core, from approximately $-45°$ east of north in the east to almost $-75°$ east of north in the west. The Stokes I beam is shown by the filled ellipse.

map produced in the lower sideband, cleaned, and restored with a Briggs factor of 0.5.

3. RESULTS

3.1. 1.3 mm *Intensity and Polarization*

MMS 6 is resolved by the $4\farcs3 \times 3\farcs0$ BIMA map. The rms noise in the map is 17 mJy beam^{-1}. The peak intensity detected in the BIMA map is 0.5 Jy beam^{-1} (30 σ), while the integrated intensity is 0.9 Jy. This is only one-third of the flux detected in the single-dish map at 1.3 mm by Chini et al. (1997). Therefore, a significant amount of the total flux has been filtered out by the interferometer.

Figure 1 shows the detected polarization vectors in the MMS 6 core at half-beamwidth sampling. Vectors have been produced at positions where $I/\sigma_I > 3$ and $I_p/\sigma_{I_p} > 3$. Eight vectors are detected across the MMS 6 core, with none detectable toward the unnamed dust clump to the south (a >9 σ detection in intensity). The nearest distinct core previously identified to the south is MMS 7, approximately $2\farcm5$ away. Matthews et al. (2001) did note an overdensity in the JCMT 850 μm data approximately $1'$ southeast of MMS 6, but our map does not extend to that position.

Table 1 gives the values of the vectors. Systematic changes are apparent in the vectors as a function of position within the map. The position angle is observed to change gradually from approximately $-75°$ to $-45°$ from west to east across the core. Note also that the smallest values of p are detected toward the peak of the intensity map.

Figure 2 illustrates the depolarization effect as the polarization percentage declines systematically as a function of intensity. This is commonly observed in maps of polarized emission and has been observed along the axis of the Orion A filament in single-dish polarimetry at 850 μm (Matthews et al. 2001). Also shown on this plot is the polarized intensity as a function of intensity, which is invariant across the map. Thus, it appears that the depolarization is due to the fact that dust grains in high-intensity regions are not effectively aligned or that, due to changes in field orientation on scales smaller than our beam, the integrated emission from the grains is not effectively polarized.

TABLE 1

POLARIZATION DATA TOWARD MMS 6

R.A. Offset (arcsec)	Decl. Offset (arcsec)	p (%)	dp (%)	ϕ (deg)	$d\phi$ (deg)
−4.50	2.50	16.3	7.7	−69.8	9.7
−4.50	5.00	9.4	3.4	−73.7	9.0
−1.50	0.00	2.5	0.9	−74.1	10.0
−1.50	2.50	2.1	0.7	−66.8	9.8
0.00	2.50	2.8	0.7	−51.3	7.4
0.00	5.00	5.6	1.6	−45.3	7.8
1.50	2.50	5.9	2.0	−40.7	9.2
1.50	5.00	10.0	3.9	−42.4	9.6

NOTE.—All positions are relative to the pointing center of R.A.(J2000) = $05^h35^m23\overset{s}{.}489$, decl.(J2000) = $-05°01'32\farcs221$.

3.2. *Comparison to the Larger Scale Magnetic Field Geometry*

The mean position angle of the vector distribution of Figure 1 is $-58° \pm 2°$. The dispersion in the distribution is 14°. The area of the BIMA map containing the polarization detections is less than a single beam in the SCUBA (15″) or Hertz (20″) maps from JCMT and the Caltech Submillimeter Observatory (CSO), respectively. The 850 μm SCUBA vector coincident with the BIMA map has a position angle of $-39° \pm 2°$ (Matthews et al. 2001), while the 350 μm vector measured by Houde et al. (2004) has a position angle of $-52\overset{\circ}{.}8 \pm 4\overset{\circ}{.}6$ toward the position of MMS 6.

The mean of the 1.3 mm distribution agrees much better with the 350 μm value than with the 850 μm value. This is perhaps not surprising, since the BIMA value represents a mean of nine data points, while the single-dish data are both single points that are neither spatially coincident with each other nor absolutely centered on the BIMA core peak. (An average of the Stokes parameters,

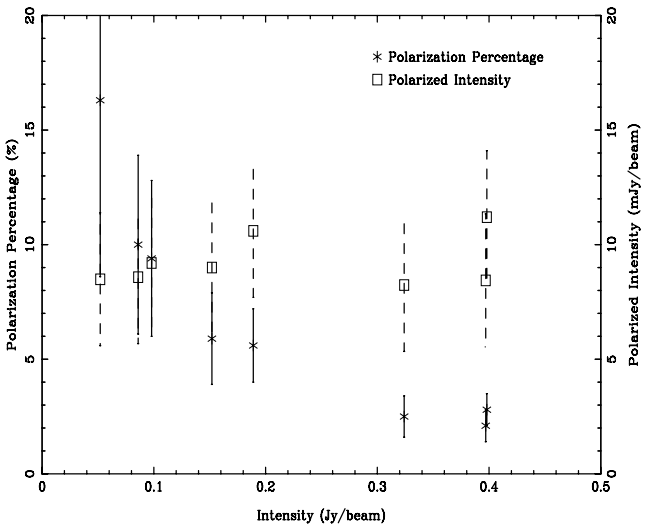

FIG. 2.—Polarized intensity (*squares*) and polarization percentage (*asterisks*) as a function of intensity in MMS 6. The polarized intensity does not vary significantly with total intensity across MMS 6. Since the polarization percentage (*asterisks*) does decline with increasing intensity, this decline must be primarily due to changes in intensity rather than in polarized intensity.

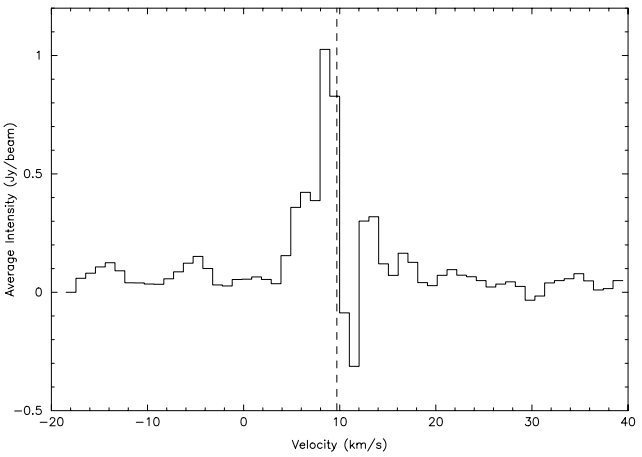

FIG. 3.—Spectrum of CO $J = 2-1$ emission from the position of the peak of the dust emission integrated over the beam area. No evidence of high-velocity gas associated with an outflow is observed. The CO emission is detected only ± 6 km s^{-1} from the velocity of the OMC-3 filament, 9.7 km s^{-1}, which is shown by the dashed line. Negative values over several channels represent the effects of missing large-scale emission in the map.

produced by convolving the data to a 15″ beam and binning to 15″ pixels, yields a single vector oriented at position angle $-55\overset{\circ}{.}3 \pm 7^{\circ}$ at an offset of 7″.5 north of the map center. This is consistent with the mean of the distribution.)

The data at the eastern edge are more consistent with the SCUBA data, while the CSO value is consistent with the mean of the vector distribution. The BIMA data trace the core, but the other data must be dominated by the filament. The lack of agreement between the single-dish data sets is in this sense more intriguing than the lack of agreement between a single-dish data set and the data of Figure 1, since the discrepancy could indicate that the field geometries probed by the different wavelengths of dust differ significantly. An alternate explanation lies in the different chop throws of the telescopes, which could produce subtle changes in the differential measure on the sky if the chop positions are significantly polarized (see the appendices of Matthews et al. [2001]).

We do not compare the polarization percentages across wavelengths, since these are subject to both a known wavelength dependence (see Hildebrand et al. [1999]) and to systematic effects of comparing single-dish and interferometric data. While the single-dish data are sensitive to all the polarized and unpolarized grains through the cloud, the BIMA data are spatially filtered and

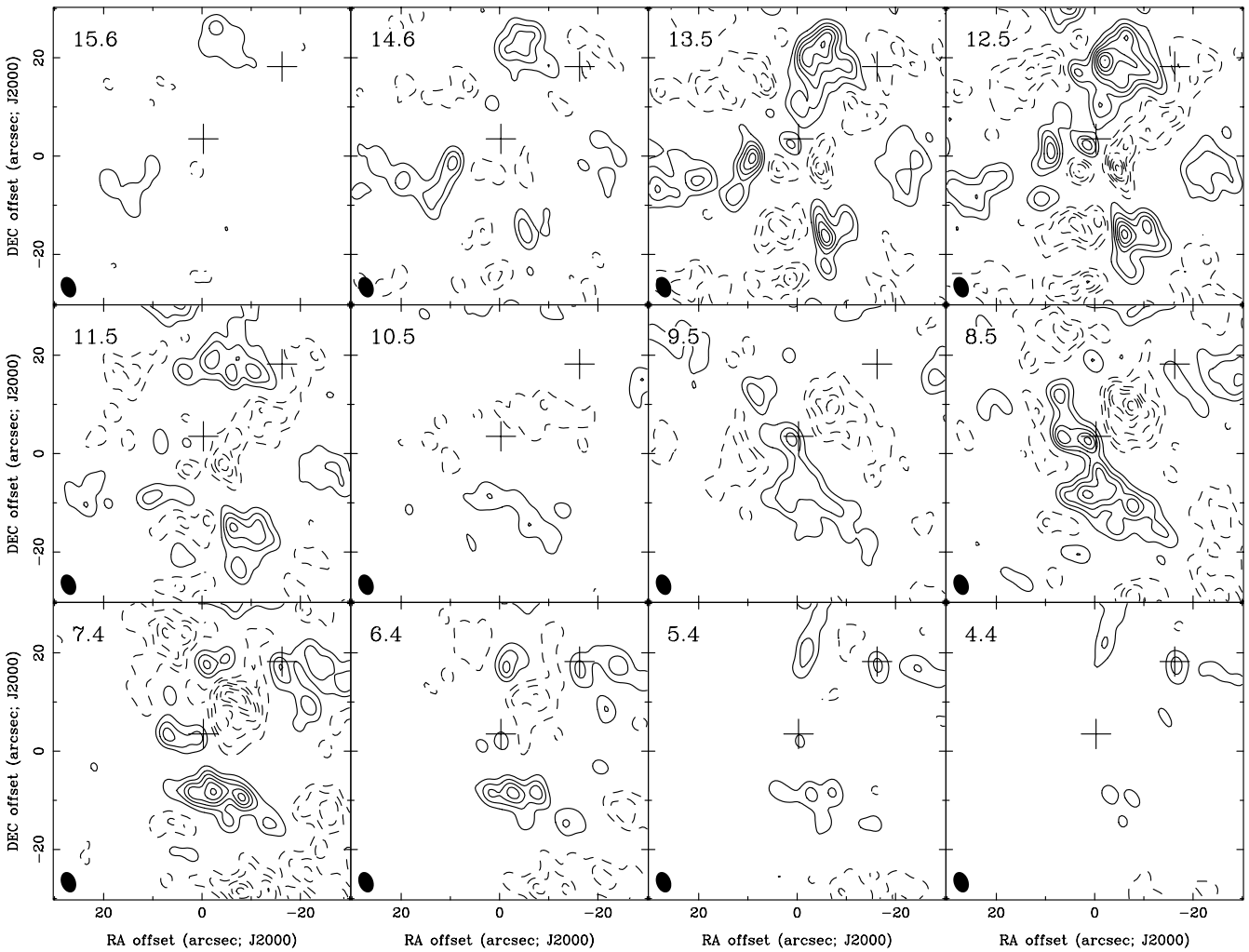

FIG. 4.—Total-intensity CO $J = 2-1$ line emission in the region surrounding MMS 6 (*central plus sign*). These are the highest resolution CO maps toward this region. The plus sign to the northwest marks the position of the MMS 5 core. Velocities are marked at the top left of each panel. CO is clearly associated with MMS 6, although the emission disappears at the velocity of the OMC-3 region (10 km s^{-1}). The MMS 5 outflow identified by Williams et al. (2003) can be seen to the east and west of that source.

preferentially probe structures matched to the interferometer's beam.

3.3. *Associated* CO *Emission*

Although MMS 6 is the brightest core in continuum emission at several wavelengths, it does not yet have a clearly identified outflow, despite many surveys of the region (Aso et al. 2000; Yu et al. 2000). No outflow could be defined even in a large CO $J = 1$–0 mosaic of the OMC-2/3 region (Williams et al. 2003). Figure 3 shows a spectrum toward the dust peak position over the beam area. No evidence of high-velocity line wings is observed. Figure 4 shows the distribution of CO $J = 2$–1 gas around the position of MMS 6. The northeast-to-southwest extension of gas around MMS 6 is consistent with the clumping of CO seen to the southeast by Williams et al. (2003) in their interferometric data, although their resolution was lower by almost a factor of 3. The clumpy nature of the gas in this region is exacerbated by the fact that the interferometer preferentially detects the high-velocity line wings, where gas is confined to small spatial scales. Williams et al. (2003) determined that their D-array BIMA data was only sensitive to 5% of the total outflow gas, since the bulk of it was distributed on scales of $1'$ or greater. Our C-array data are sensitive to a still smaller portion of the total gas. Despite the high resolution of our data set, we are likely unable to unambiguously identify an outflow from MMS 6 for this reason.

4. DISCUSSION

4.1. *Magnetic Field Strength*

It is possible under certain assumptions to estimate a field strength on the basis of the dispersion in polarization vectors in a method first described by Chandrasekhar & Fermi (1953). This method assumes that the dispersion observed in polarization angles ($d\phi$) is produced by the perturbation of the field lines by Alfvén waves. Thus, where the average density $\bar{\rho}$ and rms line-of-sight velocity $\delta v_{\rm los}$ are measured, the field strength is given by

$$B_{\rm pos} = Q\sqrt{4\pi\bar{\rho}}\frac{\delta v_{\rm los}}{d\phi}, \tag{5}$$

where Q is a *statistical* correction to the field strength derived by simulations of turbulence (Ostriker et al. 2001; Heitsch et al. 2001). The estimate of field strength is a statistical lower limit, since only the plane-of-the-sky component ($B_{\rm pos}$) of the magnetic field vector can be estimated.

We have estimated the line-of-sight velocity from N_2H^+ $J = 1$–0 observations for which the measured line widths are significantly nonthermal. The thermal velocity σ is estimated from the cloud temperature according to $\sigma = (kT/\mu m_{\rm H})^{1/2}$, where $\mu = 29$ for N_2H^+. The thermal line width is therefore 0.17 km s^{-1} for a 20 K cloud. We have adopted 20 K on the basis of the results of Chini et al. (1997), who estimate the dust temperature to be 15–25 K in MMS 6. The measured line width of the F_1, $F = 0, 1 \rightarrow 1, 2$ component of the N_2H^+ hyperfine transition is 0.4 km s^{-1} (J. Di Francesco 2004, private communication), which implies that there is a substantial nonthermal contribution to the total line width. Here $\delta v_{\rm los}$ is derived from the FWHM velocity width of an optically thin line, Δv, by the relation $\delta v_{\rm los} = \Delta v/(8 \ln 2)^{1/2}$. The rms line velocity is therefore 0.16 km s^{-1} in MMS 6.

We have estimated the mean density using the 1.3 mm continuum data of Chini et al. (1997), since it is substantially less contaminated by the presence of the surrounding filament than the 850 μm data of Johnstone & Bally (1999) and is at the same wavelength as our data set. We have not used the BIMA data to estimate the mean density of the core, since the interferometric data preferentially detects the high-density center of the core. The mean column density of H_2 is given by

$$\langle N_{\rm H_2}\rangle = \frac{S_{1.3\ {\rm mm}}}{\Omega_{1.3\ {\rm mm}}\mu m_{\rm H}\kappa_{1.3\ {\rm mm}}B(T_d)}, \tag{6}$$

where $S_{1.3\,{\rm mm}}$ is the 1.3 mm continuum flux, $\Omega_{1.3\ {\rm mm}} = (2\pi/8 \ln 2) \times {\rm FWHM}^2$ is the beam area in steradians, $m_{\rm H}$ is the mass of a hydrogen atom, $\kappa_{1.3\ {\rm mm}}$ is the absorption coefficient of the dust, and $B(T_d)$ is the Planck function.

For a 20 K core observed at 230 GHz, $B(T_d) = 2.4 \times 10^{-13}$ ergs cm^{-2} s^{-1} Hz^{-1} sr^{-1}. The beam of the IRAM 30 m telescope is $11''$ at 230 GHz; therefore, $\Omega = 3.2 \times 10^{-9}$ sr. Finally, we have taken $\kappa_{1.3\ {\rm mm}} = 0.01$ cm^2 g^{-1}, which is a value appropriate for Class 0 protostars (Ossenkopf & Henning 1994), and $\mu = 2.33$. The integrated flux of the MMS 6 core at 1.3 mm is 2.7 Jy (over an aperture of $18''$), while the peak flux is 2 Jy. Taking the total flux divided by the aperture area, we derive an average flux density of 1.01 Jy beam^{-1}, which is representative of the mean column density through the core. Thus, we derive $\langle N_{\rm H_2}\rangle = 3.4 \times 10^{23}$ cm^{-2} using equation (6). By further assuming that the depth is comparable to the observed width of the core ($\sim 10^{17}$ cm), we derive a mean number density of 3.4×10^6 cm^{-3}, which is typical of protostellar cores. This number density corresponds to a mass density of 1.2×10^{-17} g cm^{-3}. The radius of the core is 3000 AU, and its dust mass is 3 $M_\odot$.

We note that a similar treatment of the BIMA data presented here yields a significantly higher number density estimate of 1.05×10^7 cm^{-3}. This value is 3 times greater than that derived from the single-dish data. We have opted to use the density estimate of the single-dish data because the omission of lower density material (e.g., in the outer envelope) affects the mean density value. There could be systematic effects on $d\phi$ as well due to the use of interferometric polarization vectors alone in a case in which evidence of changing field geometry exists from large to small scales. However, this is not ostensibly the case in OMC-3 and MMS 6 (see § 3.2).

There are several systematic effects that influence the dispersion of the polarization vectors. First, the vectors shown in Figure 1 and listed in Table 1 are not independent, which produces a smoothing effect and minimizes the dispersion measurement. Second, we have also noted a systematic shift in the vectors, but we have not attempted to fit that variation due to the paucity of data points, which leads to an overestimation of the dispersion estimate. Third, the dispersion has not been corrected for the estimated measurement uncertainty, which means that the dispersion estimate is inflated from its true value.

With the limited S/N of this data set, there are too few vectors to be able to estimate the dispersion in beamwidth-sampled vectors. However, we can make a simple correction for the measurement uncertainties in position angle, which are on the order of 10° (see Table 1). This correction can be quantified ($\delta\phi^2_{\rm act} = \delta\phi^2_{\rm meas} - d\phi^2$) and decreases the dispersion measurement. The measured dispersion is 14°, so the actual dispersion estimate is $\sim 10^\circ$. The remaining factors, systematic variation and oversampled vectors, produce opposite effects on the dispersion. We adopt 10° as the dispersion estimate for the purposes of estimating a field strength.

Substituting the values of density, dispersion, and rms line velocity into equation (5) yields a plane-of-the-sky field strength of 640 μG (where Q has been taken to be 0.5 but can hold any

value of order unity).[2] We note that this estimator is an upper limit, because the true dispersion of independent vectors on this scale could be larger than 10°. However, this value is significantly lower than the minimum value derived for the FIR 5 core in the NGC 2024 filament by Lai et al. (2002), namely, 1.9 mG. (Use of the BIMA density estimate yields 1.1 mG for MMS 6 for the same Q-factor.) FIR 5 is a core similar to MMS 6 in that it is of a mass likely to form one or two stars. However, one important difference is that NGC 2024 FIR 5 powers one of the strongest outflows known, while MMS 6 shows no clear evidence of an outflow.

In contrast to the NGC 2024 region, there are no Zeeman-splitting measurements of the line-of-sight field strength, $B_{\rm los}$, toward OMC-3. However, Houde et al. (2004) recently estimated the inclination angle, α, of the total field to the line of sight along the integral-shaped filament by comparing spectra of ionic and neutral spectra. Toward MMS 6, they derive $\alpha = 72\overset{\circ}{.}6 \pm 4\overset{\circ}{.}4$, which would indicate that the field lies mainly in the plane of the sky. With our estimate of $B_{\rm pos}$ of 640 μG and adopting $\alpha = 70°$, the total field strength in this core would be 680 μG, while $B_{\rm los}$ is expected to be 230 μG.

4.2. *Energetics in MMS 6*

Using the density, line width, and magnetic field strength derived above, we can compare the gravitational, kinetic, and magnetic energy densities in the MMS 6 core. We estimate the radius R from the FWHM of the single-dish observation to be $\sim 6''$, which corresponds to 3000 AU at a distance of 500 pc. The gravitational energy density, $\langle E_G \rangle$, is the self-gravitating energy divided by the volume, which for a uniform sphere is given by

$$\langle E_G \rangle = \frac{4\pi G}{5} \rho^2 R^2, \tag{7}$$

where G is the gravitational constant. Using the radius above and the density estimated in § 4.1, we find an energy density of $\langle E_G \rangle = 4.8 \times 10^{-8}$ ergs cm^{-3}.

The kinetic energy density is given by

$$\langle K \rangle = \frac{3}{2} \rho \delta v_{\rm los}^2, \tag{8}$$

which yields a kinetic energy density of 4.6×10^{-9} ergs cm^{-3}, which is 10 times smaller than the gravitational energy density.

The magnetic energy density is

$$\langle M \rangle = \frac{B^2}{8\pi}, \tag{9}$$

where B is the total field strength. Using 680 μG, we calculate $\langle M \rangle = 1.85 \times 10^{-8}$ ergs cm^{-3} as the magnetic energy density. This is 4 times greater than the kinetic energy density and is more comparable to the gravitational energy density.

These data suggest that neither the magnetic nor the kinetic energy is sufficient alone to support this core against gravitational collapse. In consideration of the magnetic energy density alone, this core would be considered supercritical (i.e., the magnetic energy is insufficient to prevent collapse). By the virial theorem, the available support is insufficient to prevent core collapse, since $\langle M \rangle + 2\langle K \rangle < \langle E_G \rangle$ by approximately a factor of 2. However, we note that the actual field strength may in fact vary quite significantly from the value derived from the Chandrasekhar-Fermi method with the statistical correction factor Q. Given that the solution above suggests that the core is within a factor of 2 of criticality (just enough support available to halt gravitational collapse), the potential range of field strengths span values consistent with both subcritical (magnetic field significantly exceeds gravity) and supercritical solutions. With the presence of a point source at the position of MMS 6, it would have been unexpected to find the core to be less than critical.

4.3. *On the Preservation of Field Geometry from Clouds to Cores*

Now that several cores have been mapped with the BIMA array, it is possible to compare the high-resolution data with larger scale single-dish maps to determine if any trends are apparent. It is interesting to note that, within identified filamentary cloud structures, there is basic agreement between the polarization patterns of the filamentary clouds and the patterns of the protostellar cores that have formed within them. For instance, in addition to the OMC-3 data presented here, Lai et al. (2002) measured a similar polarization pattern in the FIR 5 core as had been measured with SCUBA for the NGC 2024 filament by Matthews et al. (2002). In addition, the supercritical core W51 exhibits an ordered polarization pattern at high resolution (Lai et al. 2001) that is consistent with SCUBA observations by Chrysostomou et al. (2002). The polarization pattern of the supercritical core DR 21(OH) also appears highly ordered in interferometric maps (Lai et al. 2003). This degree of order in the high-resolution interferometric data suggests that variations in field direction (i.e., "tangling") cannot explain the depolarization observed in large-scale maps. In contrast, tangling is observed in high-resolution maps of very massive cores, such as OMC-1 in the integral-shaped filament of Orion A (Houde et al. 2004; Schleuning 1998; Rao et al. 1998) and NGC 2071 IR in Orion B (Matthews et al. 2002; B. C. Matthews et al. 2005, in preparation). Hence, the depolarization observed in single-dish maps could, in these cases, be the result of these variations in polarization direction. A third scenario has been observed in the dark cloud Barnard 1, for which SCUBA observations detected systematic variations in the polarization position angle with dust column density. In this cloud, the angle in cores (above a column density threshold) differed consistently from the angle in the ambient dust (below the column density threshold).

These examples indicate that the environment of the parent cloud structure appears to have a significant impact on the longevity of the magnetic field geometry. While a larger data set is required to determine whether all protostellar cores formed in filamentary clouds inherit the larger scale local field geometry, initial results suggest that only massive (i.e., supercritical) cores such as OMC-1 and NGC 2071 IR exhibit evidence for tangled fields on the scales probed by the current generation of interferometers, and protostellar cores outside the filamentary environment may exhibit a different field orientation than the ambient material. If low-mass cores did form in filaments formed by collapse along field lines and the same field lines dictated collapse of cores, then subsequent outflows produced would show a higher degree of alignment than is observed in OMC-3 (Aso et al. 2000). Alternatively, the variation in outflow orientations may simply reflect the fact that the ordered component of the magnetic field is complex but not straight, in which case the polarization pattern produced in cores would not exhibit a simple correlation with the outflow direction. This is difficult to statistically

[2] In the absence of additional information about the field that could aid us in deriving Q (e.g., Lai et al. 2003), we adopt the statistical correction factor deduced from simulations (Heitsch et al. 2001; Ostriker et al. 2001).

test, given the few cores for which magnetic field geometry has been probed at high resolution.

5. CONCLUSIONS

We have detected polarized emission at 1.3 mm from the MMS 6 core. The data are consistent with preexisting cospatial larger scale polarization maps of the OMC-3 filament in which this core is embedded. As in the single-dish data toward this filament and other star-forming clouds and cores, we detect a depolarization toward the highest-density regions of the cloud. Coupled with the constant polarized intensity detected, this depolarization suggests that grains toward the highest-density regions may not be effectively polarized.

We have utilized the Chandrasekhar-Fermi method to obtain an upper limit to the plane-of-the-sky field strength of 640 μG toward this core. On the basis of the inclination of the field measured by Houde et al. (2004), we have deduced that the total field strength is 680 μG and that the predicted value of $B_{\rm los}$ is 230 μG. As yet, no Zeeman-splitting observations have been made toward this core. There are large systematic uncertainties in these estimates of field strength.

As with previous searches toward this region, we have not identified an outflow from this source in our CO $J = 2$–1 data. On the basis of estimates of the relative energy densities in the core, it should be undergoing gravitational collapse. The detection of the 3.6 cm source by Reipurth et al. (1999) suggests the presence of a collapsed object, but as yet its outflow remains elusive. The basic calculations of the energetics of the core support the picture of a collapsed object at its center, with our estimates of kinetic and magnetic energy density found to be not quite sufficient to halt gravitational collapse, assuming a correction factor of $Q = 0.5$ to the Chandrasekhar-Fermi estimate of the field strength. However, we note that, given the uncertainties discussed in § 4, *it is not possible to say whether MMS 6 is supercritical.*

The general finding of preservation of magnetic field geometry (as inferred from the polarization pattern) from the large-scale data is consistent with observations of the protostellar core NGC 2024 FIR 5 in the Orion B filamentary ridge and the W51 high-mass star-forming region.

We thank J. Di Francesco for access to the N_2H^+ data in advance of publication and our referee for an enthusiastic and thorough review. We also thank P. Goldsmith for a thorough reading of the text. The research of C. D. W. is supported through grants from the Natural Sciences and Engineering Research Council of Canada (NSERC). S.-P. L. is supported by a National Science Foundation (NSF) grant AST 02-28974 to the University of Maryland. R. M. C. acknowledges support from NSF grant AST 02-05810. The research of B. C. M. was supported by an NSERC Postdoctoral Fellowship and NSF grant 02-28963 to the University of California at Berkeley. The BIMA array is operated with support from the NSF under grants AST 02-28963 to the University of California at Berkeley, AST 02-28953 to the University of Illinois at Urbana-Champaign, and AST 02-28974 to the University of Maryland.

REFERENCES

Aso, Y., Tatematsu, K., Sekimoto, Y., Nakano, T., Umemoto, T., Koyama, K., & Yamamoto, S. 2000, ApJS, 131, 465
Chandrasekhar, S., & Fermi, E. 1953, ApJ, 118, 113
Chini, R., Reipurth, B., Ward-Thompson, D., Bally, J., Nyman, L.-Å., Sievers, A., & Billawala, Y. 1997, ApJ, 474, L135
Chrysostomou, A., Aitken, D. K., Jenness, T., Davis, C. J., Hough, J. H., Curran, R., & Tamura, M. 2002, A&A, 385, 1014
Crutcher, R. M. 1999, ApJ, 520, 706
Crutcher, R. M., Roberts, D. A., Troland, T. H., & Goss, W. M. 1999a, ApJ, 515, 275
Crutcher, R. M., Troland, T. H., Lazareff, B., Paubert, G., & Kazès, I. 1999b, ApJ, 514, L121
Dotson, J. L., Davidson, J., Dowell, C. D., Schleuning, D. A., & Hildebrand, R. H. 2000, ApJS, 128, 335
Girart, J. M., Crutcher, R. M., & Rao, R. 1999, ApJ, 525, L109
Heitsch, F., Zweibel, E. G., Mac Low, M.-M., Li, P., & Norman, M. L. 2001, ApJ, 561, 800
Hildebrand, R. H. 1988, QJRAS, 29, 327
Hildebrand, R. H., Dotson, J. L., Dowell, C. D., Schleuning, D. A., & Vaillancourt, J. E. 1999, ApJ, 516, 834
Houde, M., Dowell, C. D., Hildebrand, R. H., Dotson, J. L., Vaillancourt, J. E., Phillips, T. G., Peng, R., & Bastien, P. 2004, ApJ, 604, 717
Johnstone, D., & Bally, J. 1999, ApJ, 510, L49
Lai, S.-P., Crutcher, R. M., Girart, J. M., & Rao, R. 2001, ApJ, 561, 864
———. 2002, ApJ, 566, 925
Lai, S.-P., Girart, J. M., & Crutcher, R. M. 2003, ApJ, 598, 392
Matthews, B. 2003, BIMA Memo 100 (College Park: Univ. Maryland), http://bima.astro.umd.edu/memo/memo.html
Matthews, B. C., Fiege, J. D., & Moriarty-Schieven, G. 2002, ApJ, 569, 304
Matthews, B. C., & Wilson, C. D. 2002, ApJ, 574, 822
Matthews, B. C., Wilson, C. D., & Fiege, J. D. 2001, ApJ, 562, 400
Ossenkopf, V., & Henning, Th. 1994, A&A, 291, 943
Ostriker, E. C., Stone, J. M., & Gammie, C. F. 2001, ApJ, 546, 980
Rao, R. 1999, Ph.D. thesis, Univ. Illinois, Urbana-Champaign
Rao, R., Crutcher, R. M., Plambeck, R. L., & Wright, M. C. H. 1998, ApJ, 502, L75
Reipurth, B., Rodríguez, L. F., & Chini, R. 1999, AJ, 118, 983
Sault, R. J., Teuben, P. J., & Wright, M. C. H. 1995, in ASP Conf. Ser. 77, Astronomical Data Analysis Software and Systems IV, ed. R. A. Shaw, H. E. Payne, & J. J. E. Hayes (San Francisco: ASP), 433
Schleuning, D. A. 1998, ApJ, 493, 811
Welch, W. J., et al. 1996, PASP, 108, 93
Williams, J. P., Plambeck, R. L., & Heyer, M. H. 2003, ApJ, 591, 1025
Yu, K. C., Bally, J., & Devine, D. 1997, ApJ, 485, L45
Yu, K. C., Billawala, Y., Smith, M. D., Bally, J., & Butner, H. M. 2000, AJ, 120, 1974